

Pt-Mediated Reversible Reduction and Expansion of CeO₂ in Pt Nanoparticle/Mesoporous CeO₂ Catalyst: In Situ X-ray Spectroscopy and Diffraction Studies under Redox (H₂ and O₂) Atmospheres

Selim Alayoglu,^{†,‡} Kwangjin An,^{†,‡} G r me Melaet,^{†,‡} Shiyu Chen,[ ] Fabiano Bernardi,[ ] Lin Wang Wang,[ ] Avery E. Lindeman,^{†,‡} Nathan Musselwhite,^{†,‡} Jinghua Guo,^{||} Zhi Liu,^{||} Matthew A. Marcus,^{||} and Gabor A. Somorjai^{*,†,‡}

[†]Department of Chemistry University of California, Berkeley, California 94704, United States

[‡]Chemical Sciences Division, Lawrence Berkeley National Laboratory, Berkeley California 94720, United States

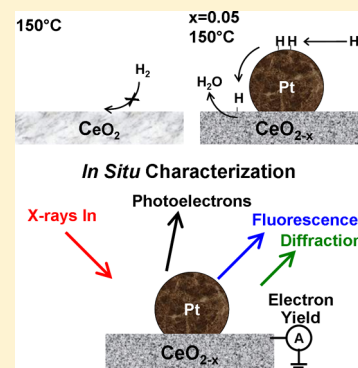
[ ]Materials Sciences Division, Lawrence Berkeley National Laboratory, Berkeley California 94720, United States

^{||}Advanced Light Source, Lawrence Berkeley National Laboratory, Berkeley California 94720, United States

[ ]Departamento de Fisica, Instituto de Fisica, Universidade Federal do Rio Grande do Sul (UFRGS), Porto Alegre-Rio Grande do Sul 90040-060, Brazil

S Supporting Information

ABSTRACT: Here, we report the Pt nanoparticle mediated reduction (oxidation) and lattice expansion (contraction) of mesoporous CeO₂ under H₂ (O₂) atmospheres and in the temperature range of 50–350  C. We found that CeO₂ in the Pt/CeO₂ catalyst was partially reduced in H₂ (and fully oxidized back in O₂) as demonstrated by several in situ techniques: APXPS spectra (4d core levels) for the topmost surface, NEXAFS total electron yield spectra (at the M_{5,4} edges) in the near surface regions, and (N)EXAFS fluorescence spectra (at the L₃ edge) in the bulk. Moreover, XRD and EXAFS showed the reversible expansion and contraction of the CeO₂ unit cell in H₂ and O₂ environments, respectively. The expansion of the CeO₂ cell was mainly associated with the formation of oxygen vacancies as a result of the Pt-mediated reduction of Ce⁴⁺ to Ce³⁺. We also found that pure mesoporous CeO₂ can not be reduced in H₂ under identical conditions but can be partially reduced at above 450  C as revealed by APXPS. The role of Pt in H₂ was identified as a catalytic one that reduces the activation barrier for the reduction of CeO₂ via hydrogen spillover.



INTRODUCTION

Ceria has been used in wide range of catalytic applications. Chemical processing, the water-gas-shift reaction,^{1–5} steam reforming,^{6–8} and the preferential oxidation of CO (PROX)^{9–12} are among the catalytic reactions that CeO₂ cocatalyzes. Moreover, CeO₂ is an oxidizing cocatalyst in automobile catalytic converters along with Pt group metal catalysts.^{13,14} Doped-ceria has also found uses as anode electrocatalyst¹⁵ and electrolyte¹⁶ in solid oxide fuel cells.

The unique defect and redox properties of CeO₂ have been identified as the stimulants that give rise to such rich chemistry.¹⁷ Redox properties of neat CeO₂ were studied in vacuum using XPS and NEXAFS spectroscopies, and Ce³⁺ was found to be dominant in the near surface regions.^{18–21}

In situ and operando studies are of utmost importance to understand the chemical and structural foundations of catalytic reactivity. From this perspective, CeO₂ has been studied under reactive gas atmospheres and (electro)catalytic reaction conditions, revealing its thermochemistry in situ. Ambient-pressure X-ray photoemission spectroscopy (APXPS) studies identified the formation of Ce³⁺ under reducing atmospheres

and at operating conditions of solid oxide fuel cells.^{22,23} The bulk reduction and lattice expansion of CeO₂ in the Cu/CeO₂ catalyst during the water-gas-shift reaction were shown by Rodriguez and co-workers by using in situ NEXAFS spectroscopy and XRD measurements.^{5,24} Davis and co-workers demonstrated the Pt loading effect on the partial (bulk) reduction of the CeO₂ cocatalyst upon H₂ treatment by using in situ NEXAFS spectroscopy and diffuse reflectance infrared Fourier transform (DRIFT) measurements.^{3,4} In accordance with their findings, Teschner and co-workers reported the partial (surface) reduction of the CeO₂ support in the presence of Pt or Pd catalysts by using APXPS under PROX conditions.^{10,11}

To date, there is no study correlating the chemical and crystallographic structures of CeO₂ during Pt-mediated reduction by H₂ in the 25–350  C range, conditions relevant to many hydrogenative hydrocarbon transformations. Here, we

Received: July 23, 2013

Revised: November 20, 2013

Published: November 21, 2013

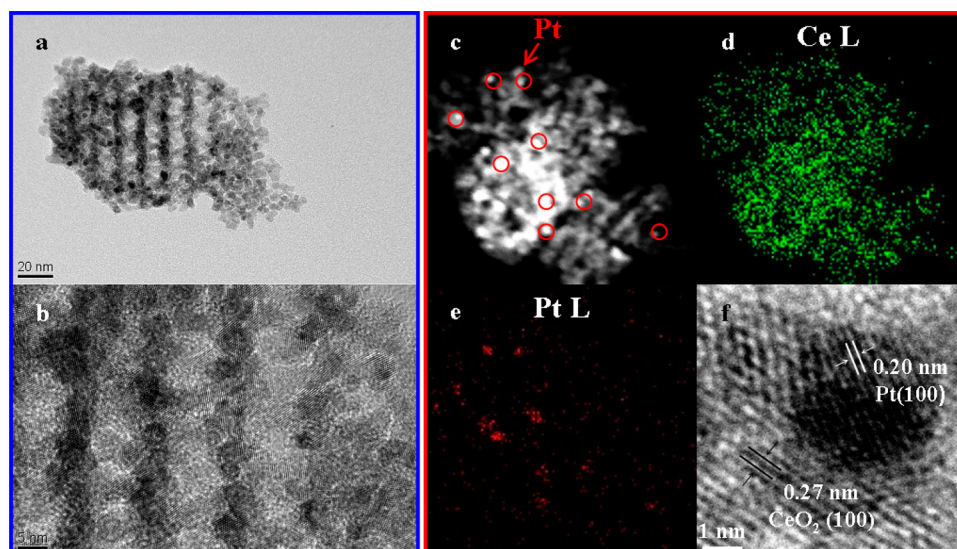


Figure 1. (a,b) TEM and (c) STEM annular dark field images and EDS elemental maps at (d) Ce and (e) Pt L lines of the Pt/CeO₂ catalyst. (f) HRTEM image showing a single Pt nanoparticle on CeO₂. Lattice planes were indexed to Pt(100) and CeO₂(100) in panel f.

report the redox chemistry and crystal structure of CeO₂ in mesoporous CeO₂ both pure and loaded with Pt nanoparticles, under (near)-ambient redox atmospheres (H₂ and O₂). To the best of our knowledge, Pt-catalyzed reversible reduction (oxidation) and expansion (contraction) of CeO₂ in the Pt/CeO₂ catalyst was recognized and elaborated for the first time by using an array of X-ray spectroscopy and diffraction tools. We found a substantial drop in the kinetic barrier for the reduction of CeO₂ in the Pt/CeO₂ catalyst in H₂ and the temperature range of 100–350 °C. We also found that the formation of O vacancy, not OH, is promoted in the presence of Pt and under H₂ atmospheres starting at ambient (25 °C) temperature. The use of X-ray spectroscopy and diffraction techniques as in situ reaction probes in this way was also utilized as an effective approach to materials characterization in heterogeneous catalysis. These studies demonstrate how an understanding of chemical and structural properties at the molecular level are needed to elucidate the universal catalytic behaviors and trends.

RESULTS AND DISCUSSION

Representative TEM images in Figure 1a,b show a single domain of mesoporous CeO₂, verifying 10 nm nanocrystalline CeO₂ grains assembled into ordered arrays with 10 nm pores. The annular dark field image and STEM/EDS elemental map at Ce and Pt L-lines in Figure 1c–e display 3 nm Pt particles dispersed in the pores of CeO₂. Figure 1f shows a single Pt particle, oriented along its (100) plane and tilted ~30° with respect to CeO₂ (100) multigrain substrate.

Chemical Composition of CeO₂ in Pure CeO₂ and Pt/CeO₂ Catalyst via APXPS. The Ce 4d core-level APXPS spectrum of neat CeO₂ in vacuum at 25 °C showed Ce⁴⁺ and no apparent Ce³⁺. The spectrum was measured at a photon energy of 380 eV and probed the Ce within 0.8 nm of the surface.

The peak envelope is consistent with that of the CeO₂ single crystal reported by Mullins and co-workers.²⁵ For the quantification of Ce 4d XPS spectra, a protocol recently developed by Liu and co-workers²⁶ was carried out due to the multielectron effects in the 4d photoionization of Ce: spin–

orbit doublet at 120–130 eV was employed as a measure of Ce⁴⁺ fraction because the photoelectrons leading to the peak envelope at 105–120 eV are highly correlated. The Ce³⁺ fraction was evaluated by subtracting Shirley background and calculating the ratio of the peak areas underneath the spin–orbit doublet at 120–130 eV and the peak envelope at 105–130 eV (Figure S2, Supporting Information). The results are plotted in Figure 3 for various conditions. For mesoporous CeO₂, our analysis indicated $4 \pm 0.4\%$ atom Ce³⁺ under 0.13 mbar (100 mtorr) O₂ and at 350 °C. Evacuating the chamber and introducing 0.13 mbar of H₂ at 350 °C into the chamber did not produce any remarkable change in the chemical composition of the topmost surface as evident in Figure 2a. Again in H₂, Ce³⁺ concentration increased to $6 \pm 0.3\%$ and $11 \pm 0.3\%$ atom at 450 and 550 °C, respectively (Figure 3a).

A new chemistry emerged when Pt nanoparticle loaded mesoporous CeO₂ (Pt/CeO₂ catalyst) was exposed to H₂ atmosphere under identical conditions. In Figure 2b, we compare Ce 4d level APXPS spectra for Pt/CeO₂ under H₂ and O₂ atmosphere at 0.13 mbar and 350 °C. The fraction of Ce³⁺ increased in H₂ at the expense of Ce⁴⁺ (see also Figure S2, Supporting Information). Furthermore, the Ce 4f valence level XPS spectrum in Figure 2c indicated a new band at about 2 eV in H₂ compared to O₂. This feature fell within the band gap of CeO₂ and hence was attributed to Ce³⁺. We evaluated the Ce³⁺ concentration under various conditions for the Pt/CeO₂ catalyst as in pure mesoporous CeO₂. The key results are as follows: (i) in O₂ and at 150 °C, there was $5 \pm 0.4\%$ atom Ce³⁺ on the topmost surface; (ii) in H₂ under identical conditions, Ce³⁺ increased to $19 \pm 0.7\%$ atom (iii) and kept increasing with increasing temperature to a maximum of $36 \pm 0.3\%$ atom at 350 °C; (iv) when switched back to O₂ at 350 °C, Ce³⁺ dropped to the starting $4 \pm 0.3\%$ atom, demonstrating the reversibility under the given conditions.

We attributed this phenomenon to the spillover of atomic hydrogen (denoted H) from Pt to CeO₂ surface, and the subsequent reduction of the CeO₂ cell. Briefly, Pt dissociates H₂ to H, which then spills onto the CeO₂ at the interface. Because H atom is reactive and mobile on the surface, it

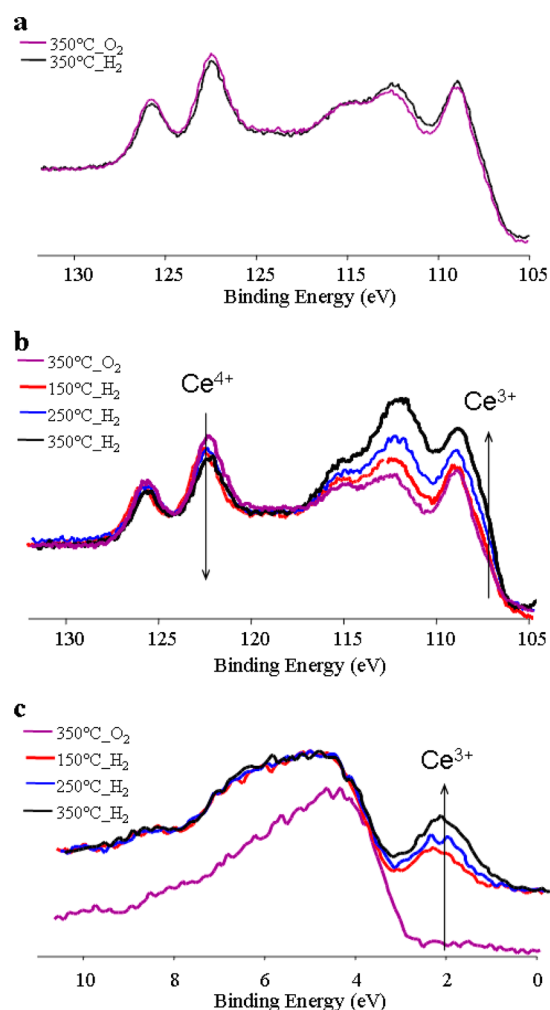
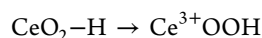
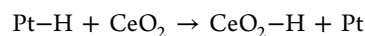
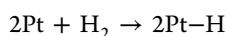
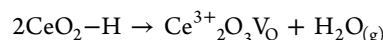


Figure 2. Ce 4d core level XPS spectra of (a) neat mesoporous CeO₂ and (b) the Pt/CeO₂ catalyst. (c) Ce 4f valence level XPS spectra of the Pt/CeO₂ catalyst. The spectra were obtained in 0.13 mbar of H₂ or O₂ and at various temperatures. Photon energy was 380 eV. Arrows in panel b show the positions of Ce³⁺ (4d_{7/2}) and Ce⁴⁺ (4d_{7/2}) at 108 and 123 eV, respectively. Arrow in panel c shows the position of Ce³⁺ located in the bandgap of CeO₂.

reduces CeO₂ forming OH or O vacant sites (denoted as V_O), according to



or



Furthermore, a semilogarithmic plot for the formation of Ce³⁺, measured by using APXPS, as a function of reciprocal temperature is shown in Figure 3c, indicating a substantial drop in activation energy for the reduction of CeO₂, from 215 kJ/mol over pure CeO₂ to about 60 kJ/mol over Pt/CeO₂ catalyst. Hence, the role of Pt is, through H-spillover, to reduce the kinetic barrier for the reduction of CeO₂.

Chemical Composition of CeO₂ in Pure CeO₂ and Pt/CeO₂ Catalyst via NEXAFS. NEXAFS total electron yield (TEY) spectra of the M_{5,4} edges, probing the near surface

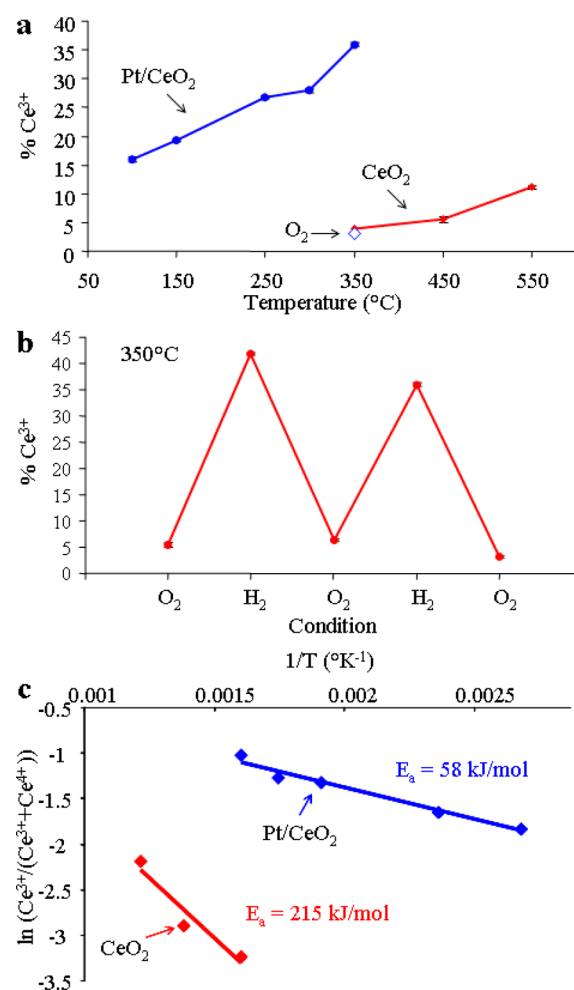


Figure 3. (a) Plots of % atom Ce³⁺ in Pt/CeO₂ (blue) and pure mesoporous-CeO₂ (red), measured by APXPS, as a function of temperature in 0.13 mbar of H₂. (b) Plot of % atom Ce³⁺ in Pt/CeO₂ versus redox condition at 350 °C. Photon energy was 380 eV. (c) Semilogarithmic plots of the fraction of Ce³⁺, defined as Ce³⁺/(Ce³⁺ + Ce⁴⁺) from APXPS, and inverse temperature (K⁻¹) for pure CeO₂ and the Pt/CeO₂, indicating the activation energies for the reduction of CeO₂ in the respective catalysts.

regions of a few nanometers, demonstrated the reduction of CeO₂ under ambient pressures of H₂ (20 mbar), mediated again by the Pt (Figure 4). Low energy M_{4,5} features, consistent with those of the Ce³⁺ reference,^{27,28} are apparent in the

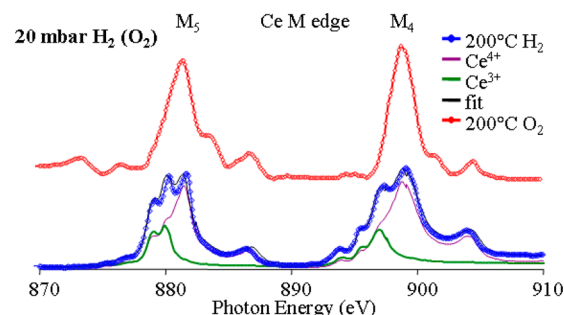


Figure 4. NEXAFS TEY spectra at the Ce M_{5,4} edge obtained at 200 °C and in 20 mbar of O₂ (red) or H₂ (blue). A sample linear combination fit (black) and Ce³⁺ (green) and Ce⁴⁺ (purple) components are shown for the reduced Pt/CeO₂.

NEXAFS spectrum obtained in H_2 at 200 °C. The linear combination fit using the reference CeAl_2 (Ce^{3+}) and CeO_2 (Ce^{4+}) indicated about $26 \pm 1\%$ atom Ce^{3+} at 200 °C and about $34 \pm 1\%$ atom Ce^{3+} at 250 °C.

We also looked into the fluorescence yield detection, which corresponds to a bulk measurement, to elucidate the extent of reduction. NEXAFS fluorescence yield (FY) spectra of the Ce L_3 edge demonstrated the reduction of mesoporous CeO_2 assisted by supported Pt nanoparticles (Figure 5). It also

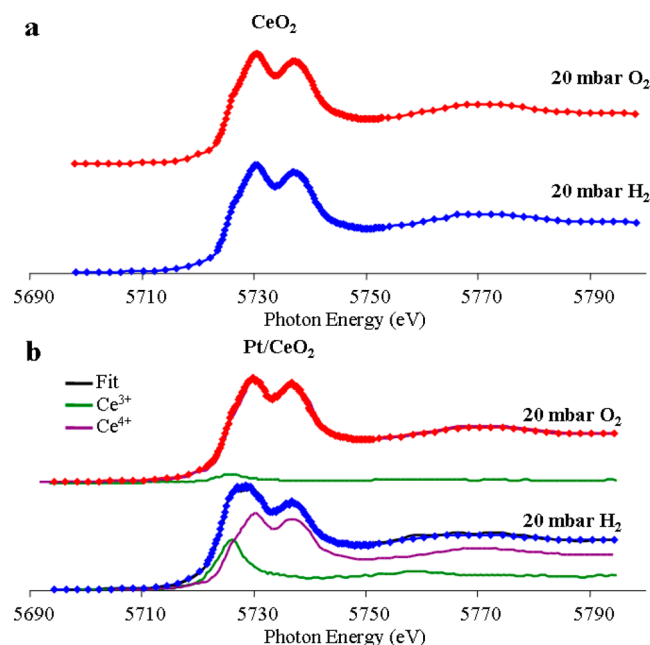


Figure 5. NEXAFS FY spectra of Ce L_3 edge for (a) pure mesoporous CeO_2 and (b) Pt/ CeO_2 catalyst obtained in 20 mbar of O_2 and at 150 °C (red) and 20 mbar of H_2 at 350 °C (blue). Note that CeO_2 has a shoulder near the Ce^{3+} energy even when fully oxidized. Also shown in panel b are sample linear combination fittings of the Ce K-edge NEXAFS spectra for the Pt/ CeO_2 catalyst obtained under 20 mbar of O_2 and H_2 , respectively. Ce^{3+} and Ce^{4+} components as well as the fits are indicated.

revealed that the reduction of CeO_2 was not limited to the surface regions. FY spectra were obtained under 20 mbar of H_2 or O_2 . In H_2 and at 150 °C, a lower energy shoulder appeared in the FY spectra, which kept growing with increasing temperature until 350 °C (see Supporting Information Figure S3).

The atomic percentage (% atom) of Ce^{3+} was calculated from the linear combination fitting of the reference Ce compounds (Figure 5b). Results of this evaluation are plotted versus the temperature in Figure 6. Under oxygen conditions and 50 °C, it was found that the bulk contains $3 \pm 1\%$ atom Ce^{3+} . As soon as the sample is exposed to 20 mbar of H_2 under identical temperature conditions, the amount of Ce^{3+} in the bulk dramatically increased to $17 \pm 2\%$ atom. Furthermore, Ce^{3+} concentration grew almost linearly with temperature and reached a maximum of $30 \pm 3\%$ atom at 350 °C. These values quantitatively agree with the results reported by Munoz et al. on Pd/Gd-doped CeO_2 nanotubes.²⁹ The oxidation state of CeO_2 in the bulk exhibited complete reversibility upon cycling between redox gases at 250 °C as shown in Figure 6b, a phenomenon identical to one observed by APXPS on the topmost surface. Moreover, a control experiment, done on Pt

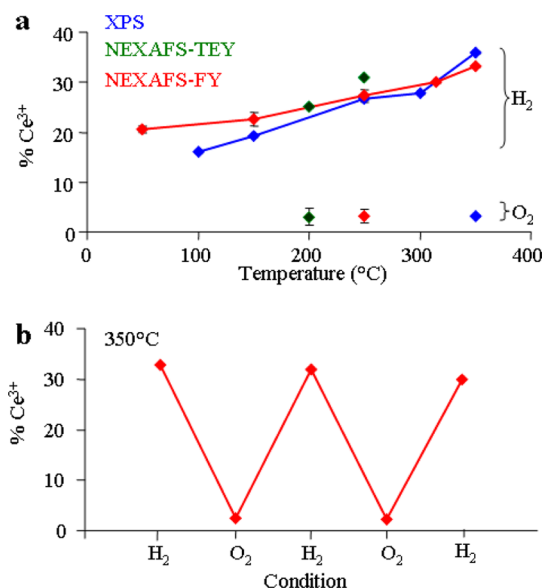


Figure 6. Plots of % atom Ce^{3+} of the Pt/ CeO_2 catalyst as a function of (a) temperature, measured by APXPS in 0.13 mbar (red) or NEXAFS in the FY (blue) and TEY (green) modes in 20 mbar; (b) redox conditions, measured by NEXAFS (FY), at 350 °C. In panel a, O_2 and H_2 spectra are displayed by solid markers or dots connected by lines, respectively. Note that Ce^{3+} concentrations were invariably low (>5%) under O_2 atmospheres and at temperatures between 150 and 350 °C for all the techniques studied.

free CeO_2 , did not show any significant change in the FY signal under identical conditions (50 to 350 °C in 20 mbar of H_2).

Note that the Ce^{3+} concentration evaluated from the FY NEXAFS spectroscopy is slightly greater than the one obtained from APXPS. We believe that this is not only a difference in the measurement of topmost surface versus the bulk as demonstrated by the TEY NEXAFS measurements but is also due to the hydrogen partial pressure environment (about 3 orders of magnitude greater for NEXAFS measurements), which can be easily related to the chemical potential effect. Indeed, an analysis of NEXAFS results clearly indicated the near surface regions-TEY detection at Ce M edge, were slightly more reduced than the bulk-FY detection at Ce L edge, under identical conditions (Figure 6).

Crystal Structure of CeO_2 in Pt/ CeO_2 Catalyst via XRD and EXAFS. Finally, we carried out XRD, again in situ, to evaluate CeO_2 phase under redox atmospheres. According to our results, the CeO_2 crystalline structure is dynamic under redox conditions, but no change in crystalline phase was observed over the whole conditions studied. In fact, we found a reversible expansion and contraction of the CeO_2 unit cell when Pt is present. Figure 7 shows the X-ray diffraction patterns of Pt/ CeO_2 catalyst obtained under 20 mbar H_2 or O_2 and at 250 °C. Reflections in the Q ($2\pi/d$, d = d-spacing) range of $2\text{--}11 \text{ \AA}^{-1}$ were assigned to the cubic fluorite phase of CeO_2 . Reflections in the gray region were partially due to the mesoporous superstructure. We focused on the region between 5 and 6 \AA^{-1} : it is evident from these medium- Q reflections that XRD patterns shifted to lower Q values in H_2 relative to O_2 , verifying the expansion of CeO_2 cell.

In agreement with the XRD results, EXAFS oscillations indicated a lengthening of Ce–O distances (from an average of 2.31 Å to an average of 2.33 Å) upon switching the gas

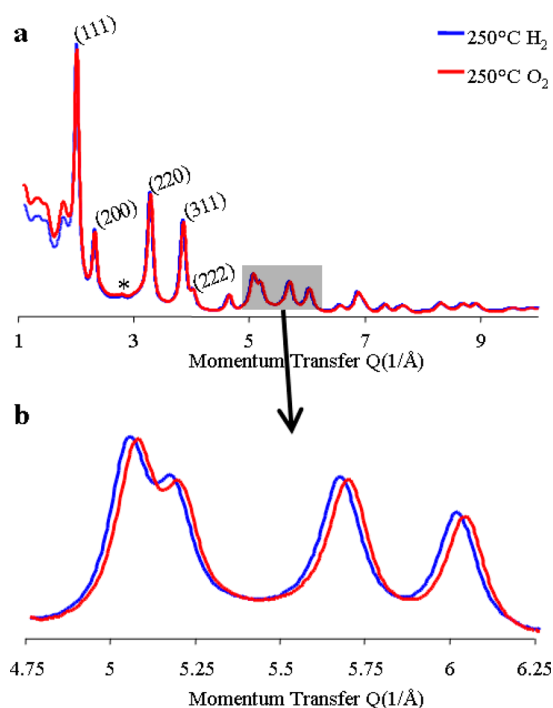


Figure 7. (a) X-ray diffraction patterns of the Pt/CeO₂ catalyst obtained in 20 mbar of H₂ (or O₂) and at 250 °C displaying the full 1–10 Å^{−1} *Q*-window. (b) X-ray reflections in the 5–6 Å^{−1} region, region marked with gray in panel (a), indicating a shift to lower *Q* values in H₂ (blue) compared to O₂ (red). Reflections in the 2–10 Å^{−1} *Q*-range were indexed to the cubic fluorite phase, and only the first five reflections are shown in parentheses. Reflections in the 1–2 Å^{−1} *Q*-range in panel a are due to background plus mesoporous superstructure. Asterisk denotes the Pt(111) reflection.

environment from O₂ to H₂ at 250 °C (see Supporting Information Figure S4).

Using full profile fitting (Rietveld analysis via GSAS) of the XRD patterns, we were able to evaluate the lattice parameter of the CeO₂ cell for each condition. The results are presented in Figure 8a. The CeO₂ cell expanded from 5.4008 ± 0.0010 Å in O₂ to 5.4094 ± 0.0007 Å in H₂ at 25 °C, corresponding to an average expansion of 0.2 ± 0.001%. Furthermore, the lattice parameter increased progressively with increasing temperature in H₂, reaching at a maximum of 5.4379 ± 0.0008 Å at 315 °C. In Figure 8a, we also plotted the thermal expansion of the CeO₂ cell as a function of temperature by using the bulk thermal expansion coefficient of CeO₂.¹⁷ At 250 °C and in 20 mbar of O₂, the measured lattice expansion fell within the line that was calculated from the thermal expansion. In H₂ under identical conditions, however, the CeO₂ cell exhibited a further expansion. Moreover, pure mesoporous CeO₂ displayed no measurable change in the lattice constant in H₂ compared to O₂ (Table S1, Supporting Information), indicating that the lattice expansions measured in H₂ atmospheres were indeed induced by Pt nanoparticles. At a constant temperature of 250 °C, we exposed the Pt/CeO₂ catalyst to a sequence of redox cycles. This experiment evidenced the total reversibility of the contraction/expansion phenomenon as shown in Figure 8b.

EXAFS oscillations also revealed a lengthening of Ce–O bond accompanied by a drop in near-neighbor coordination of Ce–O in H₂ atmospheres. Considering the drop in Ce–O coordination as a result of O vacancies, we found a linear correlation between the local Ce–O bond length change

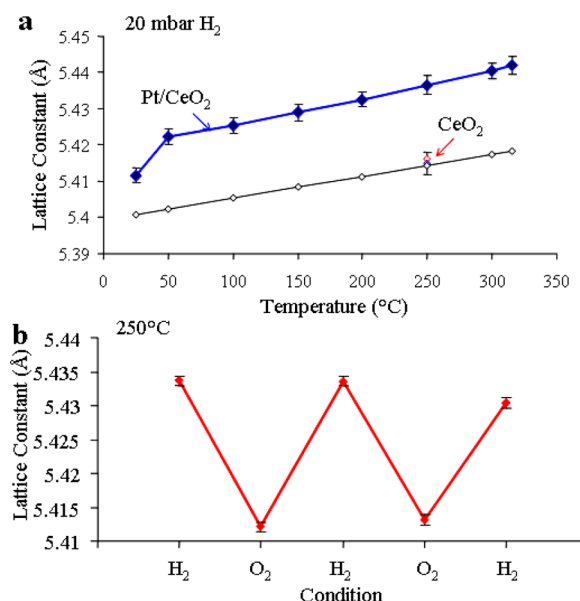
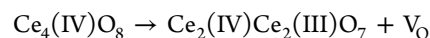


Figure 8. Lattice constant in Angstroms are plotted as a function of (a) temperature in 20 mbar of H₂ and (b) redox (H₂ or O₂) condition at 250 °C. Thermal expansion of CeO₂ cell was also plotted as a reference in panel a and shown by black circles, and the line is given as a guide to the eyes.

(%Δ*d*/*d*) and O vacancy concentration (% atom V_O) as shown in Figure 9a. The formation of Ce³⁺, which has a larger ionic radius than Ce⁴⁺ (crystal ionic radii of 115 pm versus 101 pm),²⁹ is often assigned to the expansion of reduced CeO₂. Since both the hydrogen (H) interstitial (i.e., OH) and oxygen (O) vacancy in the lattice can be attributed to the formation of Ce³⁺, we considered their contributions, separately, in the calculations. We found that the calculated lattice expansion caused by H interstitial is small compared to the experimental observation. We also found that, the calculated lattice expansion caused by O vacancy overlaps with the experimental lattice expansion. Also, a plot of % atom Ce³⁺ as a function of % oxygen vacancy in the 150–315 °C range revealed a linear correlation with a slope of exactly 4, indicating that O vacancy formation accounts for all the Ce³⁺ generated, according to the chemical equation:



This is also in agreement with exclusion of H interstitial as the main source of Ce³⁺ in the Pt/CeO₂ catalyst.

By using the thermal expansion curve in Figure 8a as reference, % expansion in the CeO₂ cell was calculated at various temperatures in H₂. The results were plotted as a function of % Ce³⁺ under identical conditions in Figure 9b and compared with the experimental results obtained from the EXAFS analysis. The absolute changes were, however, deviated from those that were found by EXAFS: given the O vacancy concentration, the local bond lengthening (EXAFS) appeared to exceed the periodic bond lengthening that was refined from Rietveld analysis (XRD). The systematic discrepancy between the two experiments can be attributed to the difference between the local short-range order, which accounts for both crystalline and noncrystalline domains, and the periodic long-range order within the nanocrystalline grains. However, it can also be considered as an anomalous structural behavior, possibly caused by increasing crystallite sizes (and crystallinity) in H₂ with

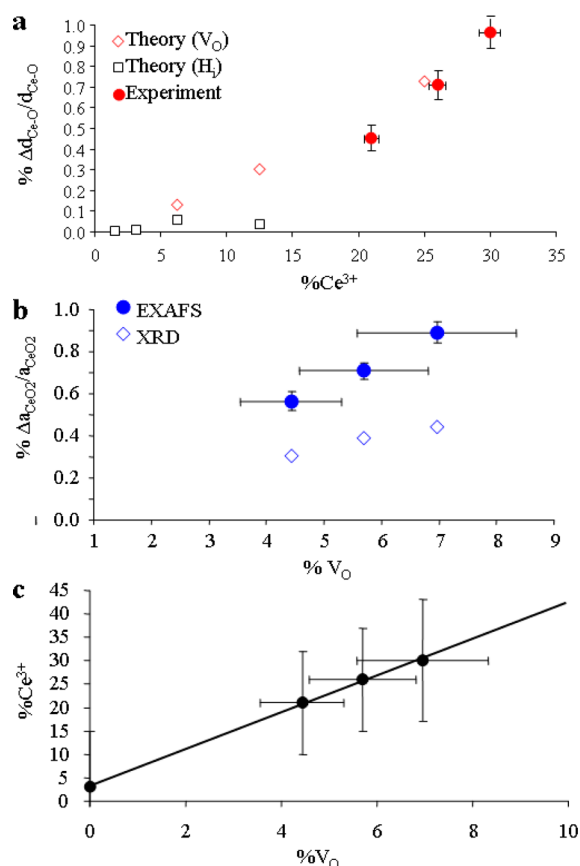


Figure 9. Plots of (a) % change in Ce–O bond length ($\% \Delta d_{\text{Ce-O}}/d_{\text{Ce-O}}$) versus % Ce^{3+} from EXAFS; (b) % change in lattice constant ($\% \Delta a/a$) versus Ce^{3+} from EXAFS and XRD; and (c) % atom Ce^{3+} versus % V_O . % changes in lattice constant and bond length were calculated by using pure CeO_2 in O_2 and at the respective temperature as reference. Lattice constants and bond lengths of pure CeO_2 were adjusted for the thermal expansion, calculated according to the formula given in ref 17. Experimental points with error bars are given by solid spheres. The ab initio calculated lattice expansion and bond lengthening are given by the open symbols: O vacancy (marked with red diamonds) and H interstitial (marked with black squares). The lattice expansion caused by H interstitial is smaller than the experimental value, and that caused by O vacancy is much larger. Solid line in panel c has a slope of 4 and indicates the theoretical $\text{Ce}^{3+}/\text{V}_\text{O}$ verifying that all Ce^{3+} comes from O vacancy in the lattice.

increasing temperature, measured by XRD. This should then counteract the tensile strain, $\Delta a/a$ by definition, to attenuate the refined (periodic) bond lengthening (see Supporting Information Figure S1).

CONCLUSIONS

In this article, we demonstrated the reversible reduction of CeO_2 in H_2 atmospheres mediated by Pt NPs supported in the pores of mesoporous CeO_2 by using synchrotron based X-ray spectroscopic and scattering techniques. APXPS spectra of the Ce 4d core levels obtained in 0.13 mbar of H_2 showed the topmost 0.8 nm progressively reduced with increasing temperature, reaching at a maximum of 36% atom Ce^{3+} at 350 °C. Likewise, near surface regions were found to be substantially reduced in 20 mbar of H_2 as verified by NEXAFS TEY spectra of the Ce $M_{4,5}$ -edges. Moreover, NEXAFS FY spectra of the Ce L-edge demonstrated that the reversible reduction extended into the bulk of CeO_2 : 18% atom Ce^{3+} measured at 150 °C

increasing linearly to 32% atom at 350 °C. XRD patterns obtained under identical conditions showed the cubic fluorite phase and no phase transformation. Nevertheless, XRD showed a reversible expansion and contraction, beyond thermal expansion, of CeO_2 cell. In H_2 atmospheres, CeO_2 lattice expanded to a maximum of 1.0% at 325 °C, where 30% atom Ce^{3+} and 7% atom V_O were found in the bulk, all simultaneously measured by (N)EXAFS spectroscopy. The lattice expansion was mainly attributed to oxygen vacancy formation in better agreement with the XRD and (N)EXAFS measurements, which also indicated structural anomalies for the mesoporous CeO_2 loaded with 3 nm Pt nanoparticles. Our findings in regards to the redox-tunable chemical and crystallographic states of CeO_2 in the Pt/ CeO_2 catalyst illustrate a unique form of metal–support interaction, which is believed to have profound implications in hydrogenative hydrocarbon transformations that Pt/ CeO_2 systems catalyze.

EXPERIMENTAL SECTION

Synthesis of Mesoporous CeO_2 . Mesoporous CeO_2 was prepared by the nanocasting approach, in which mesoporous silica KIT-6 was used as a hard-template.^{30,31} For the synthesis of KIT-6, 27 g of P123 ($(\text{EO})_{20}(\text{PO})_{70}(\text{EO})_{20}$, EO = ethylene oxide, PO = propylene oxide, Sigma-Aldrich, $M_w = \sim 5800$) and 43.5 mL of concentrated HCl were dissolved in 980 mL of water. Then, 33.3 mL of *n*-butanol was added to the solution at 35 °C with vigorous stirring.³² After 1 h, 58 g of tetraethyl orthosilicate ($\text{Si}(\text{OC}_2\text{H}_5)_4$, Sigma-Aldrich, 99%) was added to the solution followed by stirring at 35 °C for 24 h. The mixture was reacted hydrothermally at 40 °C overnight. The filtered solid was dried and calcined at 550 °C for 6 h.

For the preparation of mesoporous CeO_2 , 6.95 g of cerium(III) nitrate hexahydrate ($\text{Ce}(\text{NO}_3)_3 \cdot 6\text{H}_2\text{O}$, Sigma-Aldrich, 99%) was dissolved in 8 mL of water, then 4 g of KIT-6 and 50 mL of toluene were added to the precursor solution with stirring at 65 °C.³¹ After evaporating the toluene, the precipitated solutions were dried and calcined at 300 °C for 6 h in air. The silica template was then removed using 2 M NaOH aqueous solution heated to 60 °C, leaving the mesoporous CeO_2 , denoted as meso- CeO_2 .

Synthesis of 3 nm Pt Nanoparticles. Poly(vinylpyrrolidone) (PVP)-capped Pt nanoparticles were synthesized by polyol reduction:³³ 4 mg of $\text{H}_2\text{PtCl}_6 \cdot x\text{H}_2\text{O}$ (Sigma-Aldrich, 99.99%), 16 mg of $\text{Pt}(\text{acac})_2$ (Sigma-Aldrich, 97%), and 0.1 g of PVP (Sigma-Aldrich, $M_w = 55,000$) were dissolved in 10 mL of diethylene glycol in a 50 mL three-necked flask. The solution was heated under vacuum at 50 °C for 20 min, then heated at 245 °C for 5 min under flowing Ar. The solution was then cooled to room temperature, and an excess of acetone was poured into the solution. The precipitated nanoparticles were dispersed in ethanol.

Fabrication of Pt/ CeO_2 Catalyst. For the preparation of a 1 wt % Pt/ CeO_2 catalyst, as-synthesized Pt nanoparticles dispersed in ethanol (1 mg mL^{-1}) were added to mesoporous CeO_2 and sonicated for 3 h at room temperature.³⁴ The precipitate was separated by centrifugation and washed with acetone and ethanol four times, then dried at 80 °C.

Methods. STEM/EDS analyses were carried out using a Jeol2100F microscope equipped with an INCA energy dispersive spectrometer. The EDS analysis was carried out at 200 kV and in the scanning mode using a 1.5 nm probe.

All synchrotron studies were conducted in the Advanced Light Source at the Lawrence Berkeley National Laboratory.

Pt/meso-CeO₂ catalyst powder was pressed into a thin (~200 μm) pellet and used as-synthesized. The pellet was heated to 150 °C under He (NEXAFS spectroscopy and XRD) or in vacuum (APXPS) before the experiments. The APXPS chamber in beamline 9.3.2 has been described elsewhere.³⁵ XPS data and error analysis was carried out using CasaXPS software. NEXAFS spectroscopy was carried out in beamlines 7.0.1 (total electron yield detection at the Ce M_{4,5} edges) and 10.3.2³⁶ (fluorescence yield detection at the Ce L₃ edge). The reaction cell used in beamline 7.0.1 has been described elsewhere.³⁷ The in situ cell used in beamline 10.3.2 consists of a stainless steel body and a stainless steel lid with a 1 × 1 cm² window, which seals on the body using a Viton O-ring. A 70 μm thick Kapton membrane was hermetically sealed on the window using a silver paste. The heater components consist of a Boralectric heater element and a K-type thermocouple, located in the body and 3 mm below the window. The sample is placed above the heater element and in between two electrically isolated metal plates with 3 mm diameter holes in the center. The gas mixtures are delivered to the body using a gas manifold consisting of carefully calibrated mass flow controllers and a Baratron gauge.

We used QuickXAS mode for the data acquisition in beamline 10.3.2. Deadtime correction, pre-edge removal, postedge normalization, overabsorption correction, multielectron removal,³⁸ and linear combination fitting of the near edge spectra (up to 250 eV past the absorption threshold at the Ce L₃ edge) were carried out by employing the software at the beamline. Ce:YAG and CeO₂ were employed as Ce³⁺ and Ce⁴⁺ references, respectively. Artemis software from the IFEFFIT suite was employed to fit the EXAFS oscillations.³⁹ The EXAFS signal $k^2\chi(k)$ was extracted then Fourier-transformed using a Kaiser-Bessel window with Δk range of 5 Å⁻¹. The theoretical reference was calculated from the fluorite crystal structure (*Fm* $\bar{3}$ *m*) by using the FFEF6l code. The *R* range used in the fitting procedure corresponds to the coordination shell and goes up to 2.5 Å. Only single scattering paths were considered. All spectra were adjusted simultaneously and some constraints were included in the fitting procedure. For the FT fitting, the system was described with paths from a linear combination of two different models. Briefly, the system was described with paths from a linear combination of two different models. The first model is the usual CeO₂ with the corresponding fluorite crystal structure known. This component is supposed to have Ce–O coordination number $N_{\text{Ce-O}} = 8$, and no vacancy is allowed. The second model is represented with the same fluorite crystal structure, but it has $N_{\text{Ce-O}} = 4$ and consequently 4 vacancies for the coordination shell. The path amplitudes for the first (ceria structure with no vacancies) and second model (ceria structure with 4 vacancies) were multiplied by the weights $(1 - x_i)$ and x_i , respectively, with $x_i = ax_{3i} + b$ where i denotes the sample condition studied (temperature, gas), x_{3i} the NEXAFS-derived Ce³⁺ fraction of the sample i , and a and b the linear parameters relating the weight of the end member and the XANES derived Ce³⁺ fraction. The linear parameters a and b were used as guess parameters. The Debye–Waller factors were used as guess parameters and were different for each model (with 4 vacancies or no vacancies in the coordination shell). The variation of the Ce–O distance was scaled by the known thermal expansion¹⁷ with $\Delta R(\text{Ce}^{4+}) = \Delta R^{\text{RT}}(\text{Ce}^{4+}) + \text{thermal expansion}$, where $\Delta R(\text{Ce}^{4+})$ is the variation on the Ce–O distance for the component with no vacancies and for a given temperature, and $\Delta R^{\text{RT}}(\text{Ce}^{4+})$ is the

variation for this component at room temperature, which was used as a guess parameter. For the component with 4 vacancies, $\Delta R(\text{Ce}^{3+}) = \Delta R(\text{Ce}^{4+}) + \Delta R$ for a given condition, and ΔR is used as a guess parameter. The S_0^2 parameter was fixed at 0.74 as obtained from the fit of CeO₂ standard.

An XRD reaction cell was designed and constructed for beamline 12.2.2,⁴⁰ consisting of a 2 mm polyimide window of 25 mm diameter at the front (beam exit) and 1 mm polyimide window of 10 mm diameter at the back (beam entrance). The sample was placed 3 mm below the front window on a machined Al heating element with a 1 mm hole in the center. The cell is rated to operate in the temperature range of 25–450 °C and at pressures up to 10 bar.

The diffraction experiment was carried out in the transmission geometry using 30 keV photons. Diffraction rings were collected over a Mar345 image plate detector. Integration and calibration were performed via the Fit2D package. Sample-to-detector distance was calibrated by using a LaB₆ standard powder sandwiched between Kapton films and placed in the specimen holder.

The powder diffraction data was fitted using the Rietveld subroutine in the GSAS package.⁴¹ The assumed crystal structure was fluorite (*Fm* $\bar{3}$ *m* space group). The lattice constant, thermal displacement factor for Ce, GSAS profile terms of Lx (Lorentzian particle size broadening) and Ly (Lorentzian strain broadening), and background function were used in the fitting. The fitting parameters were tabulated in Table S2, and the isotropic thermal displacement factor of Ce, particle sizes, and % strain were plotted as a function of temperature in Figure S1, Supporting Information.

For given pressure and temperature conditions, X-ray spectra or diffraction patterns were measured, usually for an hour or more, until no further change in the spectra or diffraction pattern was observed. The acquisition time of each and every X-ray technique is, however, varied: 2 min for XRD (a bulk measurement); 20 min for NEXAFS TEY (a surface measurement); and 160 min for EXAFS (another bulk measurement). Likewise, typical exposure times for the APXPS experiments were in the order of hours during which multiple measurements, at various core and valence levels using different photon energies, were made until no further change in the spectral features could be detected. Note, that all the techniques showed the evidence of reduction (and/or expansion) of CeO₂ for the Pt/CeO₂ catalyst, starting with the first measurement, and no significant change in the course of any experiment at any given condition. This suggests that the steady-state was reached rather quickly in the time scale of any X-ray technique used. Hence, the reported Ce³⁺ (or V_O) concentrations are in steady-state levels within the time scales of X-ray experiments.

Calculation Details. The ab initio calculation of the lattice expansion is performed within the density-functional formalism as implemented in the VASP code. For the exchange-correlation potential, we used the LDA+U functional, with $U = 5$ eV for Ce *f* states.⁴² The frozen-core projector augmented-wave potentials were employed with an energy cutoff of 400 eV for plane waves and a 6 × 6 × 6 Monkhorst-Pack *k*-point mesh for the 12-atom unit cell. For the H interstitial and O vacancy in the cells, different sites are considered and the reported results are for the site with the lowest formation energy. The lattice constants and atomic positions were fully relaxed by minimizing the quantum mechanical stresses (converged to 0.1 GPa) and forces (converged to 0.01 eV/Å).

The calculated results are plotted and compared with the experimental data in Figure 9. For ideal CeO_2 , our calculated lattice constant is 5.4103 Å, which is in good consistence with the experimental value of 5.4008 ± 0.0010 Å. When a single H interstitial is produced in a 12-atom CeO_2 supercell of the cubic fluorite structure, corresponding to a chemical composition $\text{Ce}_4\text{O}_7(\text{OH})$ and 25% atom Ce^{3+} , the calculated lattice expansion is only 0.04%, much smaller than the experimental expansion, about 0.4% with 25% atom Ce^{3+} (in H_2 and at 250 °C). However, when an O vacancy is produced in a 12-atom cell, corresponding to the chemical composition $\text{Ce}_4\text{O}_7\text{V}_\text{O}$ and 50% atom Ce^{3+} , the calculated lattice expansion is as large as 1.3%, which matches the experimental value (0.8% at 50% atom Ce^{3+}) well if we extrapolate the experimental value according to the linear fit as displayed in Figure 9a. Similar calculation is also performed in a 96-atom CeO_2 supercell, which corresponds to a lower atomic percentage of Ce^{3+} (2.5% for H interstitial and 5.0% for O vacancy).

■ ASSOCIATED CONTENT

■ Supporting Information

XRD-derived plots of CeO_2 particle size and % strain, sample fittings of Ce 4d XPS spectra, additional NEXAFS FY spectra, EXAFS fittings, and tables with the refined XRD and EXAFS parameters. This material is available free of charge via the Internet at <http://pubs.acs.org>.

■ AUTHOR INFORMATION

Notes

The authors declare no competing financial interest.

■ ACKNOWLEDGMENTS

This work was supported by the Director, Office of Science, Office of Basic Energy Sciences, Division of Materials Sciences and Engineering of the U.S. Department of Energy under Contract No. DE-AC02-05CH11231. The user projects in the Advanced Light Source and Molecular Foundry at the Lawrence Berkeley National Laboratory were supported by the Director, Office of Energy Research, Office of Basic Energy Sciences of the U.S. Department of Energy under Contract DE-AC02-05CH11231. The work (theoretical calculation) is supported by JCAP, a DOE Energy Innovation Hub, under Award No. DE-SC0004993. F.B. received a research grant from CNPq-Brazil. The authors would like to thank Doctors Simon Clark, Jason Knight, Bora Kalkan, and Alastair Macdowell at beamline 12.2.2 in the Advanced Light Source for technical support, Dr. Fan Zheng for the design of EXAFS cell, and Eric Granlund for the construction of EXAFS and XRD cells.

■ REFERENCES

- (1) Bunluesin, T.; Gorte, R. J.; Graham, G. W. Studies of the Water-Gas Shift Reaction on Ceria-Supported Pt, Pd, and Rh: Implications for Oxygen-Storage Properties. *Appl. Catal., B* **1998**, *15* (1–2), 107–114.
- (2) Fu, Q.; Saltsburg, H.; Flytzani-Stephanopoulos, M. Active Nonmetallic Au and Pt Species on Ceria-Based Water-Gas Shift Catalysts. *Science* **2003**, *301* (5635), 935–938.
- (3) Jacobs, G.; Chenu, E.; Patterson, P. M.; Williams, L.; Sparks, D.; Thomas, G.; Davis, B. H. Water-Gas Shift: Comparative Screening of Metal Promoters for Metal/Ceria Systems and Role of the Metal. *Appl. Catal., A* **2004**, *258* (2), 203–214.
- (4) Jacobs, G.; Graham, U. M.; Chenu, E.; Patterson, P. M.; Dozier, A.; Davis, B. H. Low-Temperature Water-Gas Shift: Impact of Pt

Promoter Loading on the Partial Reduction of Ceria and Consequences for Catalyst Design. *J. Catal.* **2005**, *229* (2), 499–512.

- (5) Wang, X. Q.; Rodriguez, J. A.; Hanson, J. C.; Gamarra, D.; Martinez-Arias, A.; Fernandez-Garcia, M. In Situ Studies of the Active Sites for the Water-Gas Shift Reaction over Cu-CeO₂ Catalysts: Complex Interaction between Metallic Copper and Oxygen Vacancies of Ceria. *J. Phys. Chem. B* **2006**, *110* (1), 428–434.

- (6) Pino, L.; Recupero, V.; Beninati, S.; Shukla, A. K.; Hegde, M. S.; Bera, P. Catalytic Partial-Oxidation of Methane on a Ceria-Supported Platinum Catalyst for Application in Fuel Cell Electric Vehicles. *Appl. Catal., A* **2002**, *225* (1–2), 63–75.

- (7) Pino, L.; Vita, A.; Cipiti, F.; Lagana, M.; Recupero, V. Performance of Pt/CeO₂ Catalyst for Propane Oxidative Steam Reforming. *Appl. Catal., A* **2006**, *306*, 68–77.

- (8) Wanat, E. C.; Venkataraman, K.; Schmidt, L. D. Steam Reforming and Water-Gas Shift of Ethanol on Rh and Rh-Ce Catalysts in a Catalytic Wall Reactor. *Appl. Catal., A* **2004**, *276* (1–2), 155–162.

- (9) Mattos, L. V.; Noronha, E. Hydrogen Production for Fuel Cell Applications by Ethanol Partial Oxidation on Pt/CeO₂ Catalysts: the Effect of the Reaction Conditions and Reaction Mechanism. *J. Catal.* **2005**, *233* (2), 453–463.

- (10) Pozdnyakova, O.; Teschner, D.; Wootsch, A.; Krohnert, J.; Steinhauer, B.; Sauer, H.; Toth, L.; Jentoft, F. C.; Knop-Gericke, A.; Paal, Z.; et al. Preferential CO Oxidation in Hydrogen (PROX) on Ceria-Supported Catalysts, Part II: Oxidation States and Surface Species on Pd/CeO₂ under Reaction Conditions, Suggested Reaction Mechanism. *J. Catal.* **2006**, *237* (1), 17–28.

- (11) Pozdnyakova, O.; Teschner, D.; Wootsch, A.; Krohnert, J.; Steinhauer, B.; Sauer, H.; Toth, L.; Jentoft, F. C.; Knop-Gericke, A.; Paal, Z.; et al. Preferential CO Oxidation in Hydrogen (PROX) on Ceria-Supported Catalysts, Part I: Oxidation State and Surface Species on Pt/CeO₂ under Reaction Conditions. *J. Catal.* **2006**, *237* (1), 1–16.

- (12) Wootsch, A.; Descorme, C.; Duprez, D. Preferential Oxidation of Carbon Monoxide in the Presence of Hydrogen (PROX) over Ceria-Zirconia and Alumina-Supported Pt Catalysts. *J. Catal.* **2004**, *225* (2), 259–266.

- (13) Golunski, S. E.; Hatcher, H. A.; Rajaram, R. R.; Truex, T. J. Origins of Low-Temperature 3-Way Activity in Pt/CeO₂. *Appl. Catal., B* **1995**, *5* (4), 367–376.

- (14) Nunan, J. G.; Robota, H. J.; Cohn, M. J.; Bradley, S. A. Physicochemical Properties of Ce-Containing 3-Way Catalysts and the Effect of Ce on Catalytic Activity. *J. Catal.* **1992**, *133* (2), 309–324.

- (15) Fergus, J. W. Electrolytes for Solid Oxide Fuel Cells. *J. Power Sources* **2006**, *162* (1), 30–40.

- (16) McIntosh, S.; Gorte, R. J. Direct Hydrocarbon Solid Oxide Fuel Cells. *Chem. Rev.* **2004**, *104* (10), 4845–4865.

- (17) Mogensen, M.; Sammes, N. M.; Tompsett, G. A. Physical, Chemical and Electrochemical Properties of Pure and Doped Ceria. *Solid State Ionics* **2000**, *129* (1–4), 63–94.

- (18) Engelhard, M.; Azad, S.; Peden, C. H. F.; Thevuthasan, S. X-ray Photoelectron Spectroscopy Studies of Oxidized and Reduced CeO₂(111) Surfaces. *Surf. Sci. Spectra* **2004**, *11* (1), 73–81.

- (19) Hardacre, C.; Roe, G. M.; Lambert, R. M. Structure, Composition and Thermal Properties of Cerium Oxide Films on Platinum(111). *Surf. Sci.* **1995**, *326* (1–2), 1–10.

- (20) Jin, T.; Okuhara, T.; Mains, G. J.; White, J. M. Temperature-Programmed Desorption of CO and CO₂ from Pt/CeO₂: An Important Role for Lattice Oxygen in CO Oxidation. *J. Phys. Chem.* **1987**, *91* (12), 3310–3315.

- (21) Riguette, B. A.; Damyanova, S.; Gouliou, G.; Marques, C. M. P.; Petrov, L.; Bueno, J. M. C. Surface Behavior of Alumina-Supported Pt Catalysts Modified with Cerium as Revealed by X-ray Diffraction, X-ray Photoelectron Spectroscopy, and Fourier Transform Infrared Spectroscopy of CO Adsorption. *J. Phys. Chem. B* **2004**, *108* (17), 5349–5358.

- (22) DeCaluwe, S. C.; Grass, M. E.; Zhang, C. J.; El Gabaly, F.; Bluhm, H.; Liu, Z.; Jackson, G. S.; McDaniel, A. H.; McCarty, K. F.; Farrow, R. L.; et al. In Situ Characterization of Ceria Oxidation States

in High-Temperature Electrochemical Cells with Ambient Pressure XPS. *J. Phys. Chem. C* **2010**, *114* (46), 19853–19861.

(23) Zhang, C. J.; Grass, M. E.; McDaniel, A. H.; DeCaluwe, S. C.; El Gabaly, F.; Liu, Z.; McCarty, K. F.; Farrow, R. L.; Linne, M. A.; Hussain, Z.; et al. Measuring Fundamental Properties in Operating Solid Oxide Electrochemical Cells by Using in Situ X-ray Photoelectron Spectroscopy. *Nat. Mater.* **2010**, *9* (11), 944–949.

(24) Ciston, J.; Si, R.; Rodriguez, J. A.; Hanson, J. C.; Martinez-Arias, A.; Fernandez-Garcia, M.; Zhu, Y. M. Morphological and Structural Changes during the Reduction and Reoxidation of CuO/CeO₂ and Ce_{1-x}Cu_xO₂ Nanocatalysts: In Situ Studies with Environmental TEM, XRD, and XAS. *J. Phys. Chem. C* **2011**, *115* (28), 13851–13859.

(25) Mullins, D. R.; Zhang, K. Z. Metal–Support Interactions between Pt and Thin Film Cerium Oxide. *Surf. Sci.* **2002**, *513* (1), 163–173.

(26) Zhang, C. J.; Grass, M. E.; Yu, Y.; Gaskell, K. J.; DeCaluwe, S. C.; Chang, R.; Jackson, G. S.; Hussain, Z.; Bluhm, H.; Eichhorn, B. W.; et al. Multielement Activity Mapping and Potential Mapping in Solid Oxide Electrochemical Cells through the Use of Operando XPS. *ACS Catal.* **2012**, *2* (11), 2297–2304.

(27) Dong, C. L.; Augustsson, A.; Chen, C. L.; Chang, C. L.; Chen, Y. Y.; Guo, J. H. Electronic Structure and Valence State of CeAl₂ from X-ray Absorption and Emission Spectroscopy. *J. Electron Spectrosc. Relat. Phenom.* **2005**, *144*, 581–584.

(28) Munoz, F. F.; Cabezas, M. D.; Acuna, L. M.; Leyva, A. G.; Baker, R. T.; Fuentes, R. O. Structural Properties and Reduction Behavior of Novel Nanostructured Pd/Gadolinia-Doped Ceria Catalysts with Tubular Morphology. *J. Phys. Chem. C* **2011**, *115* (17), 8744–8752.

(29) Shannon, R. D. Revised Effective Ionic-Radii and Systematic Studies of Interatomic Distances in Halides and Chalcogenides. *Acta Crystallogr., Sect. A: Found. Crystallogr.* **1976**, *32* (Sep1), 751–767.

(30) Tian, B. Z.; Liu, X. Y.; Yang, H. F.; Xie, S. H.; Yu, C. Z.; Tu, B.; Zhao, D. Y. General Synthesis of Ordered Crystallized Metal Oxide Nanoarrays Replicated by Microwave-Digested Mesoporous Silica. *Adv. Mater.* **2003**, *15* (16), 1370–1374.

(31) Ren, Y.; Ma, Z.; Qian, L. P.; Dai, S.; He, H. Y.; Bruce, P. G. Ordered Crystalline Mesoporous Oxides as Catalysts for CO Oxidation. *Catal. Lett.* **2009**, *131* (1–2), 146–154.

(32) Kleitz, F.; Choi, S. H.; Ryoo, R. Cubic Ia3d Large Mesoporous Silica: Synthesis and Replication to Platinum Nanowires, Carbon Nanorods and Carbon Nanotubes. *Chem. Commun.* **2003**, *17*, 2136–2137.

(33) Rioux, R. M.; Song, H.; Hoefelmeyer, J. D.; Yang, P.; Somorjai, G. A. High-Surface-Area Catalyst Design: Synthesis, Characterization, and Reaction Studies of Platinum Nanoparticles in Mesoporous SBA-15 Silica. *J. Phys. Chem. B* **2005**, *109* (6), 2192–2202.

(34) Tsung, C. K.; Kuhn, J. N.; Huang, W. Y.; Aliaga, C.; Hung, L. I.; Somorjai, G. A.; Yang, P. D. Sub-10 nm Platinum Nanocrystals with Size and Shape Control: Catalytic Study for Ethylene and Pyrrole Hydrogenation. *J. Am. Chem. Soc.* **2009**, *131* (16), 5816–5822.

(35) Grass, M. E.; Karlsson, P. G.; Aksoy, F.; Lundqvist, M.; Wannberg, B.; Mun, B. S.; Hussain, Z.; Liu, Z. New Ambient Pressure Photoemission Endstation at Advanced Light Source Beamline 9.3.2. *Rev. Sci. Instrum.* **2010**, *81* (5), 053106.

(36) Marcus, M. A.; MacDowell, A. A.; Celestre, R.; Manceau, A.; Miller, T.; Padmore, H. A.; Sublett, R. E. Beamline 10.3.2 at ALS: a Hard X-ray Microprobe for Environmental and Materials Sciences. *J. Synchrotron Radiat.* **2004**, *11*, 239–247.

(37) Zheng, F.; Alayoglu, S.; Guo, J. H.; Pushkarev, V.; Li, Y. M.; Glans, P. A.; Chen, J. L.; Somorjai, G. In Situ X-ray Absorption Study of Evolution of Oxidation States and Structure of Cobalt in Co and CoPt Bimetallic Nanoparticles (4 nm) under Reducing (H₂) and Oxidizing (O₂) Environments. *Nano Lett.* **2011**, *11* (2), 847–853.

(38) Gomilsek, J. P.; Kodre, A.; Bukovec, N.; Skofic, I. K. Atomic Effects in EXAFS Structural Analysis of Mixed Ce Oxide Thin Films. *Acta Chim. Slov.* **2004**, *51* (1), 23–32.

(39) Ravel, B.; Newville, M. ATHENA, ARTEMIS, HEPHAESTUS: Data Analysis for X-ray Absorption Spectroscopy Using IFEFFIT. *J. Synchrotron Radiat.* **2005**, *12*, 537–541.

(40) Kunz, M.; MacDowell, A. A.; Caldwell, W. A.; Cambie, D.; Celestre, R. S.; Domning, E. E.; Duarte, R. M.; Gleason, A. E.; Glossinger, J. M.; Kelez, N.; et al. Beamline for High-Pressure Studies at the Advanced Light Source with a Superconducting Bending Magnet as the Source. *J. Synchrotron Radiat.* **2005**, *12*, 650–658.

(41) Toby, B. H. EXPGUI, a Graphical User Interface for GSAS. *J. Appl. Crystallogr.* **2001**, *34*, 210–213.

(42) Loschen, C.; Carrasco, J.; Neyman, K. M.; Illas, F. First-Principles LDA plus U and GGA plus U Study of Cerium Oxides: Dependence on the Effective U Parameter. *Phys. Rev. B* **2007**, *75* (3), 035115.